

Learning Collective Variables with Synthetic Data Augmentation through Physics-inspired Geodesic Interpolation

Soojung Yang,[†] Juno Nam,[‡] Johannes C. B. Dietschreit,^{‡,¶} and Rafael Gómez-Bombarelli^{*,‡}

[†]*Computational and Systems Biology Program, Massachusetts Institute of Technology, Cambridge, MA 02139, USA*

[‡]*Department of Materials Science and Engineering, Massachusetts Institute of Technology, Cambridge, MA 02139, USA*

[¶]*Institute of Theoretical Chemistry, Faculty of Chemistry, University of Vienna, Währinger Straße 17, 1090 Vienna, Austria*

E-mail: rafagb@mit.edu

Abstract

In molecular dynamics simulations, rare events, such as protein folding, are typically studied using enhanced sampling techniques, most of which are based on the definition of a collective variable (CV) along which acceleration occurs. Obtaining an expressive CV is crucial, but often hindered by the lack of information about the particular event, e.g., the transition from unfolded to folded conformation. We propose a simulation-free data augmentation strategy using physics-inspired metrics to generate geodesic interpolations resembling protein folding transitions, thereby improving sampling efficiency without true transition state samples. Leveraging interpolation progress parameters,

we introduce a regression-based learning scheme for CV models, which outperforms classifier-based methods when transition state data are limited and noisy.

1 Introduction

Molecular dynamics (MD) simulations have emerged as a powerful tool to study the complex behavior of molecular systems. However, despite their utility, MD simulations face significant challenges in efficiently exploring the vast conformational space of macromolecules and capturing rare events that occur on timescales beyond the reach of conventional simulation methods. Rare events, such as protein folding, ligand binding, chemical reactions, and large-scale conformational changes, play a pivotal role in numerous biological and chemical phenomena.^{1,2} These events often involve transitions between multiple metastable states separated by high free energy barriers, such that the timescales associated with rare events can be orders of magnitude longer than those accessible to standard MD simulations, rendering direct observation impractical with reasonable computational resources. Consequently, accurately characterizing the kinetics and thermodynamics of such rare events remains an important challenge.

To facilitate the efficient sampling of rare events, researchers have developed a diverse array of enhanced sampling techniques,³ which bias the simulations towards regions of interest or lower energy barriers. These techniques can roughly be divided into two classes: one that focuses the sampling of transitions by manipulating the initial conditions and the other that introduces a bias term to the potential energy surface (PES). In this work, we concentrate on the latter class of algorithms, which encompasses a broad spectrum of methodologies, including umbrella sampling,⁴ metadynamics,⁵ and adaptive biasing force.^{6,7} All of them have in common that they require the selection of one or several collective variables (CVs), special degrees of freedom that describe the rare event of interest, such that biasing along these CVs will greatly accelerate the observation of the rare transitions.

For small molecular systems, it is often possible to choose a CV based on chemical intuition, e.g., the distance between two atoms whose bond is broken or formed during a chemical reaction. In contrast, when dealing with complex high-dimensional systems, it is virtually impossible to choose a CV based on a physical basis. As an example, the dissociation of table salt in water is insufficiently described by the sodium–chloride distance, as the surrounding water molecules play an important role.^{8,9} Here, data-driven approaches can be and have been leveraged to identify a coordinate suitable for enhanced sampling.^{10–15} Machine learning techniques have been employed to map high-dimensional and general descriptors, such as C_α – C_α distances or contact maps, to lower-dimensional CVs utilizing available data, often obtained from metastable states through unbiased simulations. Sultan and Pande¹¹ proposed using distances to the decision boundary, predicted from binary classifier models, as CVs describing transitions between two states. However, learning the decision boundary between states may not suffice for effective CVs in enhanced sampling, as thorough exploration within metastable states is also crucial. Targeted Discriminant Analysis (TDA), as proposed by Trizio and Parrinello¹⁶, addresses this challenge by fitting each known state into Gaussian distributions with predefined target mean and variance. Consequently, the model learns the meaningful variances within and between states.

However, machine-learned models of CVs are data-hungry, and in the absence of information about the transition state ensemble (TSE), such data-driven CVs may not be optimal. Hence, we are faced with a chicken-and-egg problem; we need enough samples of the rare event in order to obtain good CV models that are required to perform enhanced sampling of said event. To circumvent this problem, recent methods, such as Deep-TICA¹⁷ and TPI-Deep-TDA,¹⁸ adopt an iterative approach as illustrated in Figure 1, where they first perform enhanced sampling with suboptimal CVs to collect initial trajectories, including a few transitions, and then use those samples to improve the CV. While such methods have been proven to reduce the total simulation time required to obtain the target observable, the initial simulation for the data collection would have to be long enough to observe enough

transitions. In complex systems, this step alone could be too costly.

Another caveat of utilizing classifier-based methods like those mentioned above is the requirement for accurate class labels, which may not always be readily available. Methods such as TPI-Deep-TDA,¹⁸ which treat the TSE as just another state, necessitate clear differentiation between all states. Yet, without sufficient knowledge of the system, making this distinction can be challenging. Recently, France-Lanord et al.¹⁹ introduced a regression approach based on committor probabilities. However, a drawback of this approach is its computational cost, as it requires multiple shooting simulations per data point to compute the committor probability. Even a recent CV-free approach, as introduced by Sípka et al.²⁰, also requires resampling of the transitions between the metastable states to iteratively improve the biasing potential, thus it also has a large learning cost prior to production runs.

Recently, geodesic interpolation methods have been developed to interpolate approximately to the transition path between two molecular conformations through purely geometric means. Zhu et al.²¹ proposed a Riemannian manifold based on a physics-inspired metric that effectively constructs a coarsened approximation of the PES. The geodesic interpolations on this manifold closely resemble the minimum energy paths (MEPs) on the PES. They demonstrated that these synthetic MEPs could serve as initial paths for subsequent nudged elastic band (NEB) optimization,²² ultimately bringing the initial MEP guess closer to the ground truth. Diepeveen et al.²³ introduced a metric specifically designed to accommodate large-scale protein conformational changes and developed an algorithm that renders geodesic interpolation computationally feasible. They additionally demonstrated that these interpolations closely resemble MD trajectories. While initially proposed as a method for analysis and visualization of protein structural ensembles, we demonstrate its application to the enhanced sampling.

To significantly reduce the computational cost of training effective CV models, we propose a strategy for simulation-free data augmentation. Utilizing the Riemannian manifold for protein conformations proposed by Diepeveen et al.²³, we generate geodesic interpola-

tions, which resemble protein folding transitions remarkably well. We show that augmenting training data with these interpolations improves the sampling even without the true transition state samples. Another key advantage of these interpolations is that the interpolation parameter $t \in [0, 1]$ represents the progress of the transition. This opens the door to supervised learning of protein folding in a regression setting, providing the model with richer information compared to discriminant analysis-based methods. Our experiments reveal that our regression model outperforms discriminant analysis when dealing with limited transition state samples from simulation. Our main contributions are:

- We propose an effective, simulation-free data augmentation strategy for CV learning in a protein folding context that significantly reduces the need for expensive simulations.
- When transition state data is scarce, we propose a novel regression-based learning scheme for CV models. This approach exploits the progress parameter of geodesic interpolations as a supervisory signal, leading to a better performance compared to discriminant analysis methods.

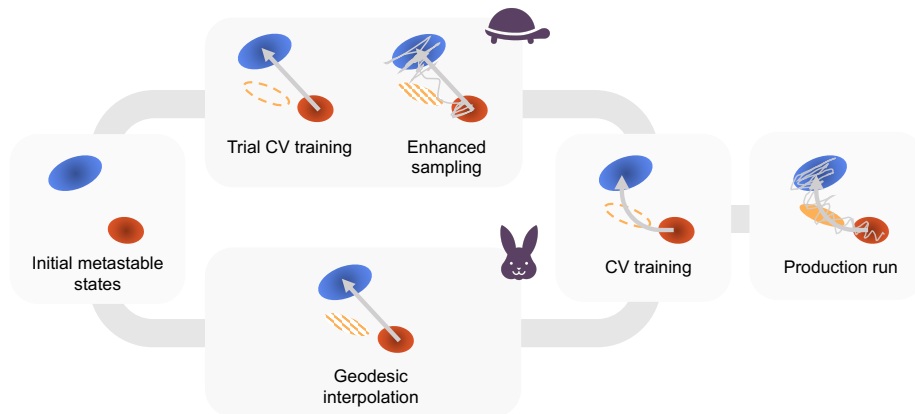


Figure 1: Depiction of a common pipeline of data-driven CVs. Initially, only data from metastable states are available (left). Long and costly production runs are meaningful only when performed with a reliable CV (right). Top (previous methods): A trial CV is trained and then iteratively improved through enhanced sampling simulations, which generate more data on the transition between the metastable states. Bottom (ours): Geodesic interpolations are used to create synthetic TSE data, from which the CV can be trained in one shot, obviating the need for an iterative procedure.

2 Methods

2.1 Geodesic interpolation of protein conformations

Here, we leverage the computationally feasible technique for approximating geodesics on Riemannian manifolds that mimic protein energy landscapes introduced by Diepeveen et al.²³ to generate synthetic transition state data by performing geodesic interpolations between metastable protein states. We summarize the geodesic interpolation approach below. For rigorous notions of Riemannian geometry, we refer to the original work.²³

The heavy atom positions (all atoms but hydrogen) of a protein structure are embedded in a point cloud manifold $\mathcal{M} \subset \mathbb{R}^{n \times 3}/E(3)$ where points do not overlap and are neither collinear nor coplanar. We equip the manifold with a distance metric $w : \mathcal{M} \times \mathcal{M} \rightarrow [0, \infty)$ defined as

$$w(\mathbf{X}, \mathbf{Y}) = \sqrt{\sum_{i < j} \left(\log \frac{\|\mathbf{x}_i - \mathbf{x}_j\|}{\|\mathbf{y}_i - \mathbf{y}_j\|} \right)^2 + \left(\log \frac{\det S_{\mathbf{X}}}{\det S_{\mathbf{Y}}} \right)^2}, \quad (1)$$

where $\mathbf{x}_i, \mathbf{y}_i \in \mathbb{R}^3$ are i -th atom positions and $S_{\mathbf{X}} = \frac{1}{n} \sum_{i=1}^n (\mathbf{x}_i - \bar{\mathbf{x}})(\mathbf{x}_i - \bar{\mathbf{x}})^{\top} \in \mathbb{R}^{3 \times 3}$ is the gyration tensor of \mathbf{X} . The implication of the metric in eq. (1) is that a change in a small pairwise distance is more significant than a change of the same magnitude in a large pairwise distance. In other words, a perturbation of the Euclidean distance between two atoms affects the distance on the manifold more strongly when the atoms were originally close by. This aligns with the physical intuition that the important interactions between the particles in a system are mostly local, and the perturbations in the interactions correspond to changes in the energy of the system.

Now, the interpolation between two structures $\mathbf{X}, \mathbf{Y} \in \mathcal{M}$ with weights $(t, 1 - t)$ is given by the w -geodesic $\gamma_{\mathbf{X}, \mathbf{Y}}^w : [0, 1] \rightarrow \mathcal{M}$ defined as

$$\gamma_{\mathbf{X}, \mathbf{Y}}^w(t) = \operatorname{argmin}_{\mathbf{Z} \in \mathcal{M}} \left(\frac{1-t}{2} w(\mathbf{X}, \mathbf{Z})^2 + \frac{t}{2} w(\mathbf{Z}, \mathbf{Y})^2 \right), \quad (2)$$

so that the interpolated structure $\gamma_{\mathbf{X},\mathbf{Y}}^w(t)$ is a minimizer of the inversely weighted sum of squared distances to the two structures.

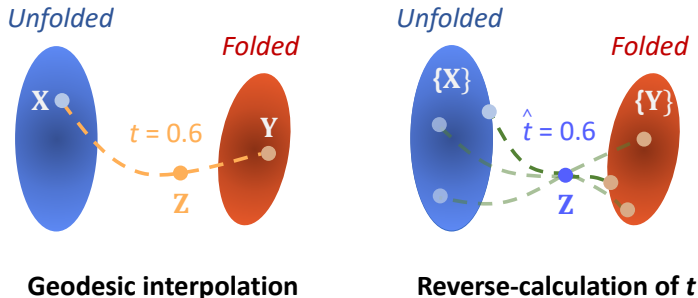


Figure 2: Left: Scheme for geodesic interpolation between unfolded and folded conformations. The interpolated structure \mathbf{Z} corresponding to interpolation parameter t is obtained using the geodesic in eq. (2). Right: Procedure to estimate interpolation parameter \hat{t} of a given intermediate conformation and sets of unfolded and folded conformations, which is given by a ratio of the minimum distances to unfolded and folded conformations (eq. (3)).

2.2 Leveraging the interpolation parameter as an indicator of reaction progress

Methods based on discriminant analysis rely heavily on accurately assigning samples to their respective states, as the loss functions are tailored to maximize the differentiation between these states. As reported in Ray et al.¹⁸, training the CV model with reduced overlap between states can significantly enhance its performance. However, in situations where our understanding of the system is limited, distinguishing samples from the metastable states and those from the TSE becomes challenging. Overlapping definition of these states can impede the effectiveness of enhanced sampling techniques, as accurate state predictions are crucial for discriminatory methods, which can be measured by their convergence to the correct reaction free energy value. To address this issue, we propose leveraging the interpolation parameter t as a proxy for the reaction progress.

As shown in eq. 2 it is always possible to find a structure $\gamma_{\mathbf{X},\mathbf{Y}}^w(t)$ that interpolates between two given samples from the metastable basins. Given an intermediate structure, however,

it is not possible to determine the value of the interpolation parameter t , as there is no information of the end-state geometries used for the interpolation. For the unlabeled data from simulations, we therefore inversely estimate the parameter \hat{t} as a ratio of the minimum geodesic distance to each metastable state as

$$\hat{t}(\mathbf{X} | \mathcal{U}, \mathcal{F}) = \frac{\min_{\mathbf{U} \in \mathcal{U}}(w(\mathbf{X}, \mathbf{U}))}{\min_{\mathbf{U} \in \mathcal{U}}(w(\mathbf{X}, \mathbf{U})) + \min_{\mathbf{F} \in \mathcal{F}}(w(\mathbf{X}, \mathbf{F}))}, \quad (3)$$

where \mathbf{F} and \mathbf{U} are samples from the set of folded and unfolded conformations, \mathcal{F} and \mathcal{U} , respectively. In the corresponding experiment, we demonstrate that incorporating \hat{t} as a label in regression learning significantly enhances model performance. See Fig. 2 for a depiction of both eqs. 2 and 3.

2.3 Chignolin as a model system

To demonstrate the capabilities of our enhanced sampling method for protein simulations, we utilize the chignolin variant CLN025 as a benchmark system. Despite its small size of 10 residues and 166 atoms, it folds into a stable β -hairpin structure. Simulating this folding process poses a non-trivial sampling challenge that necessitates very long simulation times in unbiased simulations. Hence, chignolin is recognized as a popular benchmark system for the evaluation of enhanced sampling methods. In this work, the 106- μ s long unbiased simulation trajectory of CLN025²⁴ serves as reference data for assessing the accuracy and efficiency of our CVs. An average folding time of 0.6 μ s was reported in the reference simulation for CLN025.

2.4 Transition-focused data augmentation

While simulations often generate abundant data within metastable states, capturing the rare transition state is challenging. Incorporating this scenario, we aim to train a robust CV model by utilizing the abundant metastable state data and synthetic transition state data.

We begin by extracting 1,500 frames from each metastable state from the reference trajectory, which was sampled in 200 ps intervals. Using the time vs. C_α RMSD plot, where the RMSD is computed with respect to the reference folded structure, we identify trajectory windows for both the folded and unfolded states. Within these windows, we select 1,500 consecutive frames, with a padding of a minimum of 150 frames to ensure that the selected frames are not adjacent to any transitions. Then, to mimic the transition state, we perform 3,000 geodesic interpolations between the metastable state geometries. We control the distribution of the synthetic TSE by sampling t from a target distribution. Considering the abundant data from the metastable states, we sample t from a Gaussian distribution centered at 0.5 to produce more conformations closer to the transition state, as values of t near 0 or 1 correspond to the samples belonging to the metastable states. As depicted in Figure 3(a), geodesic interpolation from an unfolded (left) to a folded (right) state yields structures (middle, opaque) resembling those from MD simulations (middle, transparent). Detailed information regarding the frame numbers, the RMSD plot, and the geodesic interpolations are provided in Section S1 of the Supporting Information (SI).

Alternatively, to mimic the limited availability of true transition state samples and compare the impact of the synthetic data augmentation with a hypothetical iterative approach, we curated 240 frames from the reference trajectory encompassing folded-unfolded transitions. We define the transition as a change from C_α RMSD $> 3 \text{ \AA}$ to C_α RMSD $< 1 \text{ \AA}$ within 2 ns (10 consecutive frames). The obtained transition samples constitute about 0.04% of the entire reference data. Given the large time window (2 ns) and the large gap between time frames (0.2 ns), these transition paths contain structures from metastable states, mirroring realistic case where state classification is challenging due to limited system knowledge.

2.5 Machine learning collective variable models

Machine-learned collective variables (ML-CV) are designed to map high-dimensional structural descriptors onto lower-dimensional CVs. For all models, we featurize the inputs with

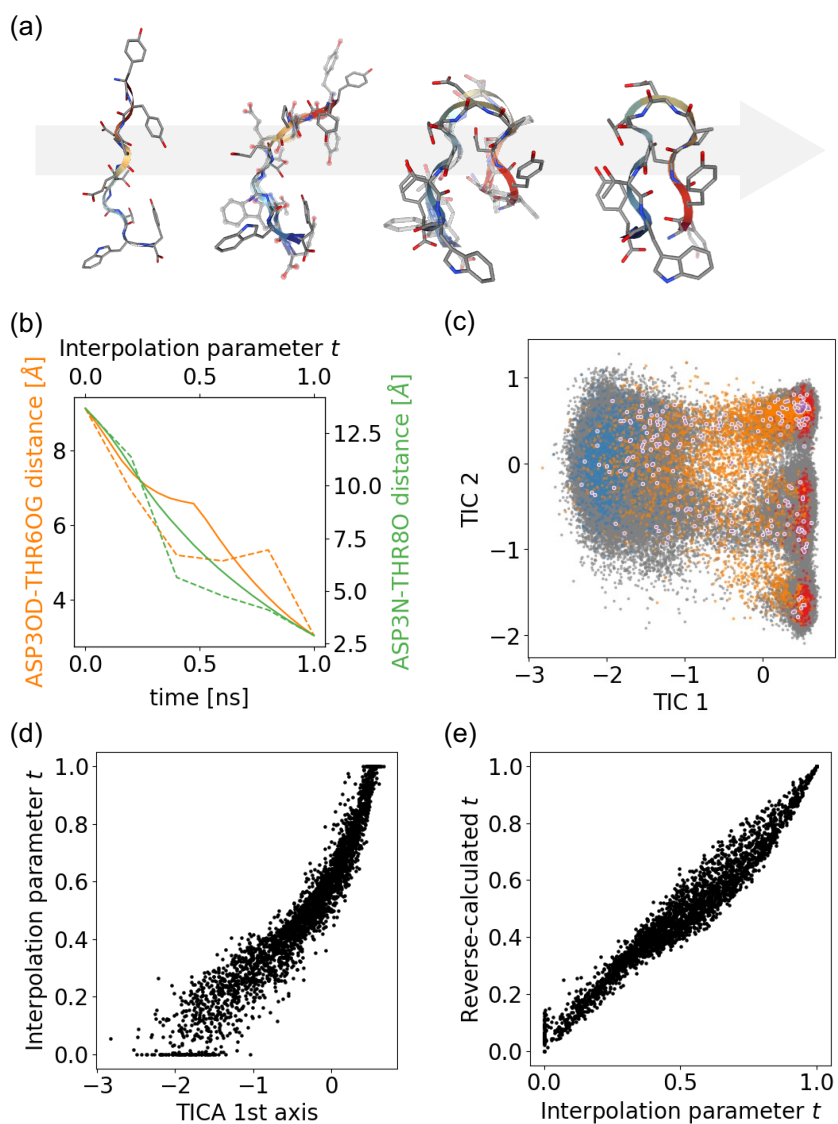


Figure 3: Comparison of the unfolded–folded transition observed in a long reference trajectory and the corresponding transition generated through geodesic interpolation of the endpoints. **(a)** Overlay of interpolated structures (opaque) and the reference structures (transparent). The initial and final structures are identical. **(b)** Evolution of the donor–acceptor distances for the two key hydrogen bonds observed in the folded state, in respective colors. The dashed lines are the reference transition as a function of time, and the solid lines are the interpolated conformations as a function of parameter t . **(c)** Overlay of the reference trajectory (gray), folded (blue), and unfolded (red) state dataset selected from the reference trajectory, transition windows from the reference trajectory (purple), and the interpolated samples (orange) on the first two slow modes from TICA. **(d)** Interpolation parameter t describes the progress along the slowest mode correlated to transition. **(e)** Interpolation parameter t can be reverse-calculated with the ratio of distances from the metastable states.

all 45 pairwise contacts between ten C_α atoms.

Given class labels for metastable state samples, discriminant analysis-based methods become a natural starting point. CV learning with targeted discriminant analysis (TDA) loss, as introduced by Trizio and Parrinello¹⁶, has proven to be effective. In the case of one-dimensional CVs, TDA assumes that there exist a non-linear transformation such that the marginal Boltzmann distribution along the CV forms a mixture of N_s Gaussians with user defined means and variances. The TDA loss is defined as shown in eq. 4, where N_s represents the total number of states, μ_k and σ_k are mean and standard deviation of CV model predictions for the training data with ground truth state label k , $\bar{\mu}_k$ and $\bar{\sigma}_k$ denote the target Gaussian mean and standard deviation corresponding to state k , and α , β are hyperparameters.

$$L_{\text{TDA}} = \alpha \sum_k^{N_s} (\mu_k - \bar{\mu}_k)^2 + \beta \sum_k^{N_s} (\sigma_k - \bar{\sigma}_k)^2 \quad (4)$$

This loss function enforces the distribution of model predictions for the training data from each metastable state closely matches the corresponding target Gaussian distribution.

We train multi-layer perceptron (MLP) models with the TDA loss, both with and without interpolated samples. The model trained solely on the two metastable states ($N_s = 2$) is denoted as **TDA**, while the one trained on the two metastable states along with the synthetic transition state generated from geodesic interpolation is labeled as **TDA_geo** ($N_s = 3$). Additionally, we prepare a TDA model trained on the two metastable states and the transition paths extracted from the reference simulation ($N_s = 3$), referred to as **TDA_ref**.

In comparison to TDA models that are trained on class labels, we also train MLP regression models that utilize the interpolation parameter t as labels with mean squared error (MSE) loss. The regression model trained on the two metastable states together with the synthetic TSE data is named **Reg_geo**, and the one trained on the two metastable states combined with the reference transition paths is termed **Reg_ref**. Due to the large difference between the number of metastable state samples and the reference transition samples, we

implement oversampling of the reference transition data by a factor of five within the training set to maintain balanced training. More details on the model training are described in Section S1 in the SI.

2.6 Enhanced sampling and result analysis

For each ML-CV, we perform four 1- μ s WTM-eABF²⁵ simulations initiated from distinct unfolded configurations. WTM-eABF enhances the sampling along the chosen CV by effectively flattening the energy landscape with the combination of the extended-system adaptive biasing force (eABF, Fu et al.²⁶) and well-tempered metadynamics (WTM, Barducci et al.²⁷). In ABF, the negative running estimate of average force along the CV is applied to adaptively shear off the barrier, while in WTM, the adaptive potential is stacked along the CV to fill up the energy landscape to the barrier level.²⁸ We evaluate the performance of our ML-CVs by analyzing the convergence of the estimated reaction free energy of folding and the resulting PMF.

The PMF $A(s)$ is obtained as a function of CV value s from the biased simulations via MBAR analysis.^{29,30} Integrating the PMF over each metastable basin allows for the computation of the free energy difference between the folded and unfolded states:³¹

$$\Delta F = -k_{\text{B}}T \log \left(\frac{\int_{\text{folded}} \exp(-A(s)/k_{\text{B}}T) \text{d}s}{\int_{\text{unfolded}} \exp(-A(s)/k_{\text{B}}T) \text{d}s} \right). \quad (5)$$

We report the mean and standard deviation of three runs after systematically removing the outlier with the highest deviation in ΔF from the reference ΔF value at 1- μ s, ensuring a more robust and reliable assessment. The results for the same analysis but with the inclusion of the outlier are reported in Section S3 of the SI.

In addition to ΔF , we introduce the mean absolute error (MAE) of the PMF, defined as

follows:

$$\text{MAE}(A, A_{\text{ref}}) = \frac{\int |A(s) - A_{\text{ref}}(s)| \mathbb{I}[A_{\text{ref}}(s) < A_{\text{thres}}] \text{d}s}{\int \mathbb{I}[A_{\text{ref}}(s) < A_{\text{thres}}] \text{d}s}, \quad (6)$$

where $\mathbb{I}[\cdot]$ is an indicator function and $A(s)$ and $A_{\text{ref}}(s)$ are PMFs for the same CV obtained from the three enhanced sampling runs and the long reference trajectory, respectively. The PMFs are aligned by setting minimum values to zero. This metric quantifies the average difference between the two PMFs within relevant CV regions characterized by reference PMF values lower than the threshold $A_{\text{thres}} = 25$ kJ/mol. Alongside capturing the PMF difference within metastable basins, as indicated by ΔF , the PMF MAE also assesses deviations from the reference PMF in transition regions.

3 Results and Discussion

3.1 Geodesic interpolation resembles state-state transitions

In this section, we investigate the properties of the interpolated data and the parameter t . The intermediate structures generated using geodesic interpolation smoothly interpolate between the unfolded and folded structures, with a close resemblance to the unbiased reference trajectory over simulation time, as visualized in Fig 3(a). The donor–acceptor distances of the two key hydrogen bonds between Asp3–Thr6 and Asp3–Thr8 are also smoothly interpolated, following the trend of those from the unbiased trajectory (Figure 3(b)).

Time-lagged independent component analysis (TICA) is a dimensionality reduction technique that effectively diagonalizes a time-lagged correlation matrix.^{32,33} Where principal component analysis (PCA) returns eigenvectors that are linear combinations of the input features that maximize the corresponding variance, TICA returns the combinations with the slowest motions. The first component of TICA represents the slowest collective motions of the chignolin system, capturing the unfolded–folded transition, and the second component

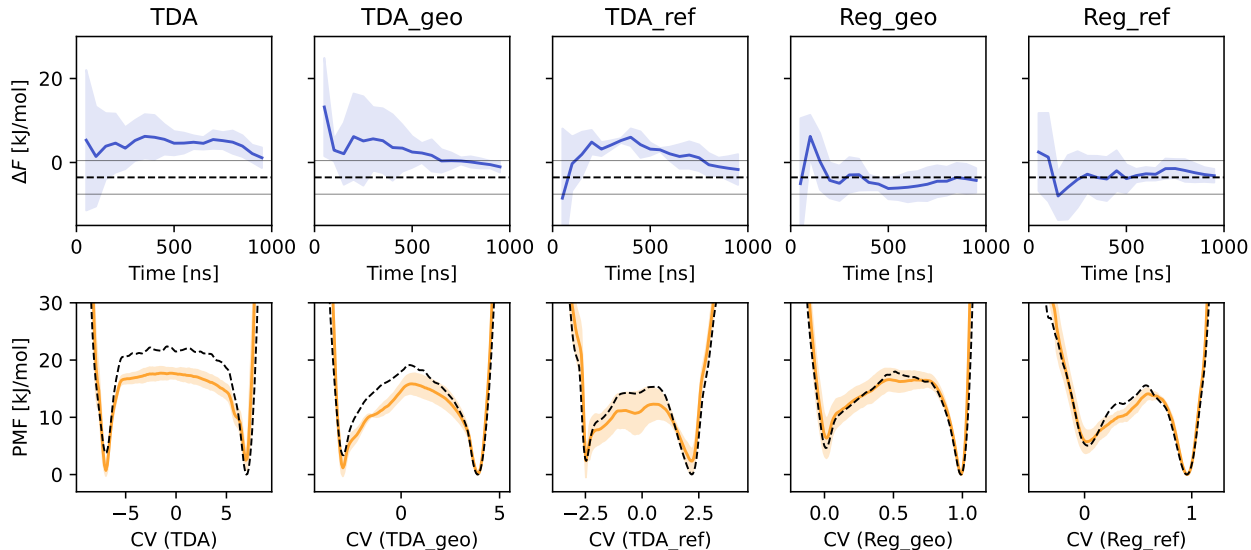


Figure 4: Convergence of the free energy difference (ΔF) between folded and unfolded state and the PMF at the end of the simulation as sampled with WTM-eABF using each CV. Top panel: Evolution of the ΔF estimate over the course of the trajectory. Solid lines indicate a ± 4 kJ/mol range (chemical accuracy) around the ΔF value obtained from the long unbiased reference runs (dashed line). Bottom panel: Comparison of reference PMF obtained by projection of reference data (dotted line) and those obtained from 1 μ s WTM-eABF simulations with the given CV. The shaded areas represent the standard deviation of three independent simulations.

resolves the three clusters within the folded state. Figure 3(c) shows that the interpolated structures and the reference transition paths have very similar projections on the first two time-lagged independent components (TICs). Furthermore, as shown in Figure 3(d), the interpolation parameter t has a strong correlation with the slowest mode of the system (TIC 1), indicating that t is in fact a useful descriptor of the progress of chignolin folding.

Although t approximates the ratio of geodesic distances to the two structures, information about the original structures is lost and cannot be backtracked from the interpolated structure. This requires the approach presented in eq. (3), where we compute the geodesic distance between the point of interest and all samples within each metastable state, selecting the minimum values to establish the distance ratio. Despite this loss of endpoint information, we observe a strong correlation between the original t and the reverse calculated \hat{t} , as illustrated in Figure 3(e). This reliable reverse calculation of the interpolation parameter

enables us to map any conformation to its corresponding progress along the reaction coordinate, thereby supporting the use of regression-based CVs trained on the TSE labeled with reverse-calculated interpolation parameters.

Table 1: Mean free energy of folding (ΔF) obtained from 1- μ s WTM-eABF simulations (Figure 4) with the corresponding reference value from the long unbiased simulation, and the mean absolute error of the potential of mean force (PMF MAE, eq. (6)) for each CV. Values in parentheses are the standard deviation from three independent simulations. All values are reported in units of kJ/mol.

CV	ΔF	ΔF_{ref}	PMF MAE
TDA	1.12 (2.44)	-3.58	4.97 (1.10)
TDA_geo	-1.04 (1.34)	-3.53	3.08 (0.53)
TDA_ref	-1.68 (3.65)	-3.58	3.20 (1.14)
Reg_geo	-4.27 (2.93)	-3.56	2.44 (0.54)
Reg_ref	-3.16 (1.61)	-3.56	2.07 (0.28)

3.2 Data augmentation improves ML CV

From the three statistically independent 1- μ s WTM-eABF enhanced sampling simulations, with the first 50 ns discarded as equilibration time, we obtained the PMF and calculated the free energy of folding (ΔF , eq. (5)) as a function of simulation time. The convergence of ΔF and the final PMFs obtained from the enhanced sampling runs are reported in Figure 4. We further compare the sampled PMFs with those obtained from the reference trajectory by investigating the difference between ΔF and the reference value ΔF_{ref} and evaluating the PMF MAE (eq. (6)), collected in Table 1.

First, the ΔF_{ref} values obtained from the projection of the reference trajectory onto the CV lie within a very narrow range of -3.58 to -3.53 kJ/mol. This consistency indicates that all of our trained CVs can correctly distinguish between the unfolded and folded equilibrium conformations in the reference trajectory. Additionally, we classified the conformations into folded, transition, and unfolded states based on the number of hydrogen bonds characteristic

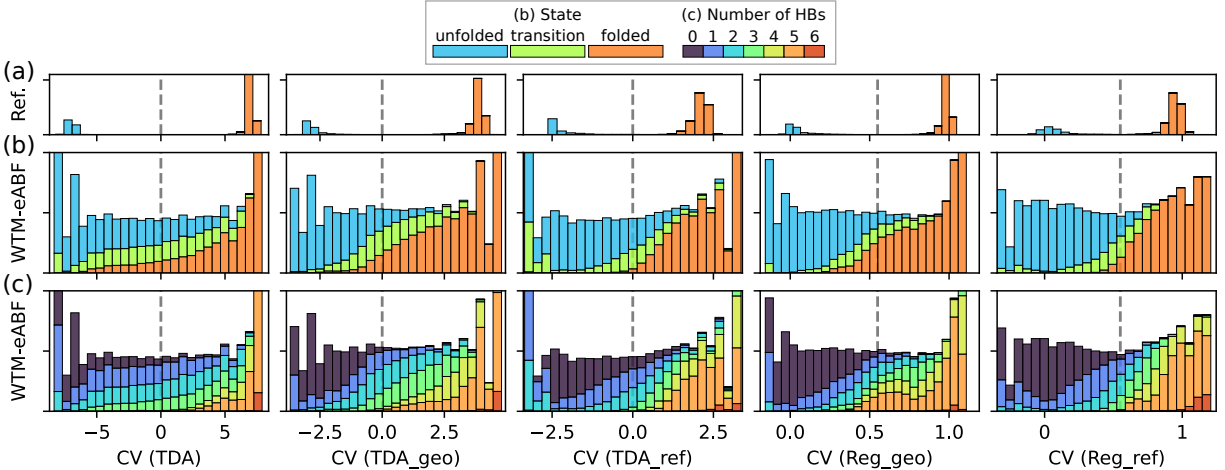


Figure 5: Distribution of conformational states along the collective variables. **(a)** Unbiased reference run state distribution, **(b, c)** Distribution of conformational states and the number of folded state hydrogen bonds in WTM-eABF runs, respectively. The hydrogen bonds present in the folded state are defined in Fig. S2, and conformational states are categorized as folded, transition, and unfolded based on a two-hydrogen-bond threshold. Each plot includes a vertical boundary line indicating the location of the potential of mean force maximum along the respective CVs.

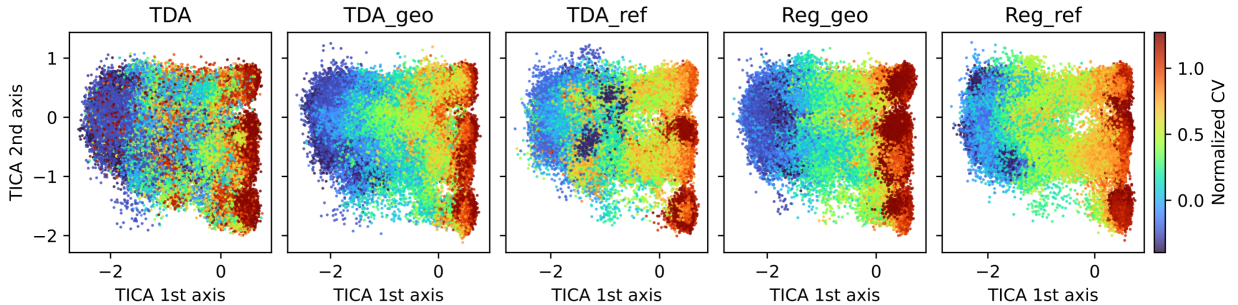


Figure 6: Projections of the conformations from the WTM-eABF enhanced sampling trajectory using different CV models onto the first two time-lagged independent components, colored based on the normalized CV value. The CV values were scaled such that the PMF minima of the unfolded and folded basins correspond to 0 and 1, respectively.

of the folded state, as detailed in the SI. The distribution of conformational states along the CV, depicted in Figure 5(a), confirms that the projections from each metastable state are separated into distinct regions of CV values.

Figure 4 and Table 1 show that models trained with data augmentation (**TDA_geo** and **Reg_geo**) outperform the model trained solely on metastable state conformations (**TDA**).

Both **TDA_geo** and **Reg_geo** successfully approach the reference value of ΔF within the chemical accuracy threshold of 4 kJ/mol. Notably, **Reg_geo** quickly converges to the reference ΔF in less than 250 ns and demonstrates a very good reproduction of the reference PMF. While the default **TDA** model seems to approach the reference ΔF , it fails to fall within the chemical accuracy range of the reference value. The corresponding **TDA** PMF shows fair agreement within the folded and unfolded basins, but exhibits a large deviation along the transition region.

The enhancement in performance from the data augmentation can be attributed to the CV model’s ability to generalize its classification ability to off-equilibrium conformations observed in the enhanced sampling runs and accurately identify the transition progress. This is evident in the CV projections of conformations from the WTM-eABF runs shown in Figure 5(b). For **TDA_geo** and **Reg_geo**, the conformations are more distinctly separated along the CV axis compared to **TDA**, where a notable portion of misclassified samples (unfolded conformations in the folded region of the CV and vice versa, as well as unfolded and folded conformations in the transition region of the CV) are observed. Figure 6 further illustrates the classification ability of each model. Unlike the data-augmented models, **TDA** exhibits noticeable misclassified conformations where the transition region is partially assigned with folded and unfolded regions of the CV. The misclassification by the **TDA** model is the root cause of the underestimation of transition barrier, as it wrongly assigns low-energy metastable state conformations to this region. It has to be noted that all CV models correctly identify the states of the equilibrium conformations, while the results for off-equilibrium conformations show a large discrepancy according to the training data. This underscores the importance of ensuring robustness to out-of-distribution configurations through training with data augmented with TSE structures, which is efficiently achieved by the interpolation scheme in this work.

3.3 Regression model is effective with scarce transition data with noisy class labels

In this section, we compare the performance of discrimination-based and regression-based models in the low-transition-data regime, in line with the common enhanced sampling scenarios where transition data is limited. The **TDA_ref** and **Reg_ref** models are trained with TSE structures extracted from the reference trajectory, which are 12.5 times fewer than the synthetic geodesic interpolations.

The results in Figure 4 and Table 1 demonstrate that ***_ref** models perform comparatively to their corresponding ***_geo** models, implying that the synthetic dataset can enhance the models similarly to the real data. Notably, the superior performance of **Reg_geo** model compared to the **TDA_geo** model extends to the scarce-data regime, as evidenced by **Reg_ref** outperforming **TDA_ref**.

The differences in performance can be explained by the conformational state distribution depicted in Figure 5(b) and Figure 6. While the **Reg_ref** CV successfully distinguishes the off-equilibrium conformational states, with a well-defined transition region aligned to the PMF maximum, **TDA_ref** projects an appreciable portion of the transition conformations onto CV values corresponding to the metastable state conformations. This behavior causes the enhanced sampling protocol to explore high-energy off-equilibrium transition state conformations in the metastable state regions rather than low-energy conformations, resulting in an undersampling of the metastable basins and incorrectly lowering PMF barrier of the transition. This ablation study demonstrates the effect of richer information given to regression models: the regression target t serves as a supervisory signal that is strongly correlated with the reaction progress. As a result, **Reg_ref** shows better separation between the two metastable states and the TSE compared to its classifier counterpart, **TDA_ref**.

4 Conclusion

We developed a scheme to train collective variables (CVs) from metastable state configurations using the geodesic interpolation to generate a synthetic transition state ensemble (TSE). We found that the generated TSE closely aligns with the reference transition configurations and provides additional information of the transition progress via the interpolation parameter t . By sampling the parameter from a predefined distribution, we could control the distribution of the generated TSE over the transition progress. Furthermore, we devised a method to reverse calculate the interpolation parameter, enabling the incorporation of the known transition data. By leveraging the interpolation parameter label as a regression target for CVs, we demonstrated notable improvements in the enhanced sampling simulation results when compared to the CVs trained solely on metastable state conformations. These results highlight the importance of incorporating transition state information into CV model training. This not only enhances the ability to accurately distinguish between the metastable states, but also enables to effectively capture the underlying dynamics of the system, as evidenced by the change in a number of hydrogen bonds along the CV axis. We emphasize that geodesic interpolation is not exclusively limited to protein conformations but can be generalized to a broader spectrum of rare events. We anticipate that further development of this method would be applicable in various chemical events, ranging from study of folding pathways of larger proteins to modeling complex chemical reactions.

Acknowledgement

The authors acknowledge the MIT SuperCloud and Lincoln Laboratory Supercomputing Center for providing HPC resources that have contributed to the research results reported in this article. The authors thank D. E. Shaw Research for sharing the reference trajectory data of Chignolin (CLN025) in Lindorff-Larsen et al.²⁴. We also want to thank Martin Šípka for helpful discussions. S.Y. is supported by Takeda Fellowship and Ilju Overseas PhD

Fellowship. J.C.B.D. is is thankful for the support of the Leopoldina Fellowship Program, German National Academy of Sciences Leopoldina, grant number LPDS 2021-08.

Supporting Information Available

The SI contains: i) the details of the molecular dynamics and enhanced sampling simulations; ii) the specifics of the data augmentation using geodesic interpolation and CV training; iii) a structure-based analysis using hydrogen bonds present in the folded state; iv) further simulation analysis with TICA and PCA projections; v) complete ΔF /PMF analysis results with the outlier included.

References

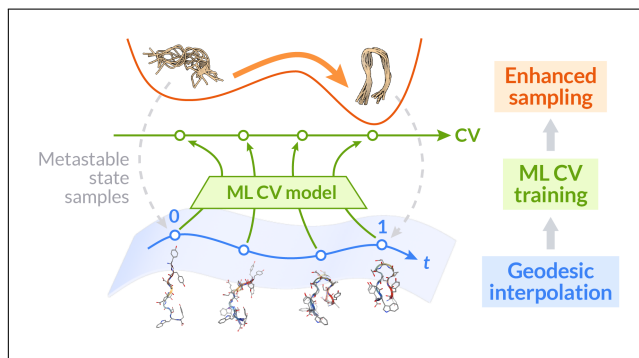
- (1) Chipot, C.; Pohorille, A. *Free Energy Calculations. Theory and Applications in Chemistry and Biology*; Springer Verlag, 2007.
- (2) Peters, B. *Reaction rate theory and rare events*; Elsevier, 2017.
- (3) Hénin, J.; Lelièvre, T.; Shirts, M. R.; Valsson, O.; Delemotte, L. Enhanced sampling methods for molecular dynamics simulations. *arXiv preprint arXiv:2202.04164* **2022**,
- (4) Torrie, G. M.; Valleau, J. P. Nonphysical sampling distributions in Monte Carlo free-energy estimation: Umbrella sampling. *Journal of Computational Physics* **1977**, *23*, 187–199.
- (5) Laio, A.; Parrinello, M. Escaping free-energy minima. *Proceedings of the National Academy of Sciences of the United States of America* **2002**, *99*, 12562–12566.
- (6) Darve, E.; Pohorille, A. Calculating free energies using average force. *Journal of Chemical Physics* **2001**, *115*, 9169–9183.

- (7) Comer, J.; Gumbart, J. C.; Hénin, J.; Lelièvre, T.; Pohorille, A.; Chipot, C. The adaptive biasing force method: Everything you always wanted to know but were afraid to ask. *The Journal of Physical Chemistry B* **2015**, *119*, 1129–1151.
- (8) Geissler, P. L.; Dellago, C.; Chandler, D. Kinetic Pathways of Ion Pair Dissociation in Water. *J. Phys. Chem. B* **1999**, *103*, 3706–3710.
- (9) Wang, R.; Mehdi, S.; Zou, Z.; Tiwary, P. Is the local ion density sufficient to drive NaCl nucleation in vacuum and in water? 2023; <http://arxiv.org/abs/2309.09284>, arXiv:2309.09284 [physics].
- (10) Mendels, D.; Piccini, G.; Parrinello, M. Collective Variables from Local Fluctuations. *Journal of Physical Chemistry Letters* **2018**, *9*, 2776–2781.
- (11) Sultan, M. M.; Pande, V. S. Automated design of collective variables using supervised machine learning. *Journal of Chemical Physics* **2018**, *149*.
- (12) Wang, Y.; Ribeiro, J. M. L.; Tiwary, P. Past–future information bottleneck for sampling molecular reaction coordinate simultaneously with thermodynamics and kinetics. *Nature Communications* **2019**, *10*.
- (13) Bonati, L.; Rizzi, V.; Parrinello, M. Data-Driven Collective Variables for Enhanced Sampling. *Journal of Physical Chemistry Letters* **2020**, *11*, 2998–3004.
- (14) Sun, L.; Vandermause, J.; Batzner, S.; Xie, Y.; Clark, D.; Chen, W.; Kozinsky, B. Multitask machine learning of collective variables for enhanced sampling of rare events. **2020**, 1–10.
- (15) Šípka, M.; Erlebach, A.; Grajciar, L. Constructing Collective Variables Using Invariant Learned Representations. *Journal of Chemical Theory and Computation* **2023**,
- (16) Trizio, E.; Parrinello, M. From enhanced sampling to reaction profiles. *The Journal of Physical Chemistry Letters* **2021**, *12*, 8621–8626.

- (17) Bonati, L.; Piccini, G.; Parrinello, M. Deep learning the slow modes for rare events sampling. *Proceedings of the National Academy of Sciences* **2021**, *118*, e2113533118.
- (18) Ray, D.; Trizio, E.; Parrinello, M. Deep learning collective variables from transition path ensemble. *The Journal of Chemical Physics* **2023**, *158*.
- (19) France-Lanord, A.; Vroylandt, H.; Salanne, M.; Rotenberg, B.; Saitta, A. M.; Pietrucci, F. Data-driven path collective variables. 2023.
- (20) Sípka, M.; Dietschreit, J. C. B.; Grajciar, L.; Gómez-Bombarelli, R. Differentiable Simulations for Enhanced Sampling of Rare Events. International Conference on Machine Learning, ICML 2023, 23-29 July 2023, Honolulu, Hawaii, USA. 2023; pp 31990–32007.
- (21) Zhu, X.; Thompson, K. C.; Martínez, T. J. Geodesic interpolation for reaction pathways. *The Journal of Chemical Physics* **2019**, *150*.
- (22) Mills, G.; Jónsson, H.; Schenter, G. K. Reversible work transition state theory: application to dissociative adsorption of hydrogen. *Surface Science* **1995**, *324*, 305–337.
- (23) Diepeveen, W.; Esteve-Yagüe, C.; Lellmann, J.; Öktem, O.; Schönlieb, C.-B. Riemannian geometry for efficient analysis of protein dynamics data. *arXiv preprint arXiv:2308.07818* **2023**,
- (24) Lindorff-Larsen, K.; Piana, S.; Dror, R. O.; Shaw, D. E. How fast-folding proteins fold. *Science* **2011**, *334*, 517–520.
- (25) Fu, H.; Shao, X.; Cai, W.; Chipot, C. Taming rugged free energy landscapes using an average force. *Accounts of chemical research* **2019**, *52*, 3254–3264.
- (26) Fu, H.; Shao, X.; Chipot, C.; Cai, W. Extended adaptive biasing force algorithm. An on-the-fly implementation for accurate free-energy calculations. *Journal of chemical theory and computation* **2016**, *12*, 3506–3513.

- (27) Barducci, A.; Bussi, G.; Parrinello, M. Well-tempered metadynamics: a smoothly converging and tunable free-energy method. *Physical review letters* **2008**, *100*, 020603.
- (28) Chipot, C. Free energy methods for the description of molecular processes. *Annual Review of Biophysics* **2023**, *52*, 113–138.
- (29) Shirts, M. R.; Chodera, J. D. Statistically optimal analysis of samples from multiple equilibrium states. *The Journal of chemical physics* **2008**, *129*.
- (30) Hulm, A.; Dietschreit, J. C.; Ochsenfeld, C. Statistically optimal analysis of the extended-system adaptive biasing force (eABF) method. *The Journal of Chemical Physics* **2022**, *157*.
- (31) Dietschreit, J. C. B.; Diestler, D. J.; Ochsenfeld, C. How to obtain reaction free energies from free-energy profiles. *The Journal of Chemical Physics* **2022**, *156*, 114105.
- (32) Molgedey, L.; Schuster, H. G. Separation of a mixture of independent signals using time delayed correlations. *Physical review letters* **1994**, *72*, 3634.
- (33) Pérez-Hernández, G.; Paul, F.; Giorgino, T.; De Fabritiis, G.; Noé, F. Identification of slow molecular order parameters for Markov model construction. *The Journal of chemical physics* **2013**, *139*.

TOC Graphic



Supporting Information:

Learning Collective Variables with Synthetic Data Augmentation through Physics-inspired Geodesic Interpolation

Soojung Yang,[†] Juno Nam,[‡] Johannes C. B. Dietschreit,^{‡,¶} and Rafael
Gómez-Bombarelli^{*,‡}

[†]*Computational and Systems Biology Program, Massachusetts Institute of Technology,
Cambridge, MA 02139, USA*

[‡]*Department of Materials Science and Engineering, Massachusetts Institute of Technology,
Cambridge, MA 02139, USA*

[¶]*Institute of Theoretical Chemistry, Faculty of Chemistry, University of Vienna, Vienna,
Austria*

E-mail: rafagb@mit.edu

Contents

S1 Computational Details	S-3
S1.1 Simulation details	S-3
S1.2 Data augmentation details	S-3
S1.3 Structural analysis	S-6
S2 Additional simulation analysis	S-7
S2.1 C_α -TICA projections of the simulated trajectories	S-7
S2.2 Analysis of the simulated trajectory in the input feature space	S-8
S3 Complete result analysis with the outlier included	S-9
S3.1 Outlier analysis of Reg_ref run	S-10
References	S-13

S1 Computational Details

S1.1 Simulation details

Molecular dynamics. Molecular dynamics simulations of chignolin (CLN025 variant) were performed with GROMACS 2023^{S1} patched with PLUMED 2.9.0.^{S2} The system was solvated in a cubic water box of size $39.61 \times 39.61 \times 39.61 \text{ \AA}^3$, and neutralized with two Na^+ ions. The protein molecule was parametrized with the CHARMM22* force field^{S3} and the water molecules with the CHARMM-modified TIP3P model^{S4} analogously to the reference simulation.^{S5} Simulations were performed in the NVT ensemble. The temperature was controlled with the velocity rescaling thermostat (v-rescale) at 340 K. The equations of motion were integrated with the leap-frog algorithm with a time step of 2 fs. The LINCS algorithm was used to constrain all bonds involving hydrogen atoms. Four independent initial configurations were prepared by sampling four different unfolded chignolin coordinates from the reference simulation and equilibrating the system for 10 ps.

Enhanced sampling parameters. We used the combination of DRR and METAD bias modules in PLUMED to perform WTM-eABF simulations, and defined machine-learned collective variables using the PYTORCH_MODEL module. We used a FRICTION of 1.0, TAU of 15 for the DRR bias and PACE of 100, HEIGHT of 0.965, BIASFACTOR of 12.765 for the well-tempered metadynamics bias. All values are reported in default PLUMED units (ps for time and kJ/mol for energy). We applied harmonic wall restraints with a spring constant of $k = 10^5$ restraining the system to explore CV values within a reasonable range. CV-specific settings are summarized in the table below:

S1.2 Data augmentation details

Extraction of folded and unfolded configuration. From the total 534,743 frames in the reference trajectory, 1,500 folded state data points were selected from the 19,000th to the

Model	DRR			METAD			Wall restraints	
	Min	Max	Spacing	Min	Max	Sigma	Lower	Upper
TDA	-9.0	9.0	0.15	-9.5	9.5	0.75	-9.0	9.0
TDA_geo	-2.5	3.0	0.05	-3.0	3.5	0.25	-2.5	3.0
TDA_ref	-3.0	2.5	0.05	-3.5	3.0	0.25	-3.0	2.5
Reg_geo	-0.4	1.3	0.01	-0.45	1.35	0.05	-0.4	1.3
Reg_ref	-0.4	1.3	0.01	-0.45	1.35	0.05	-0.4	1.3

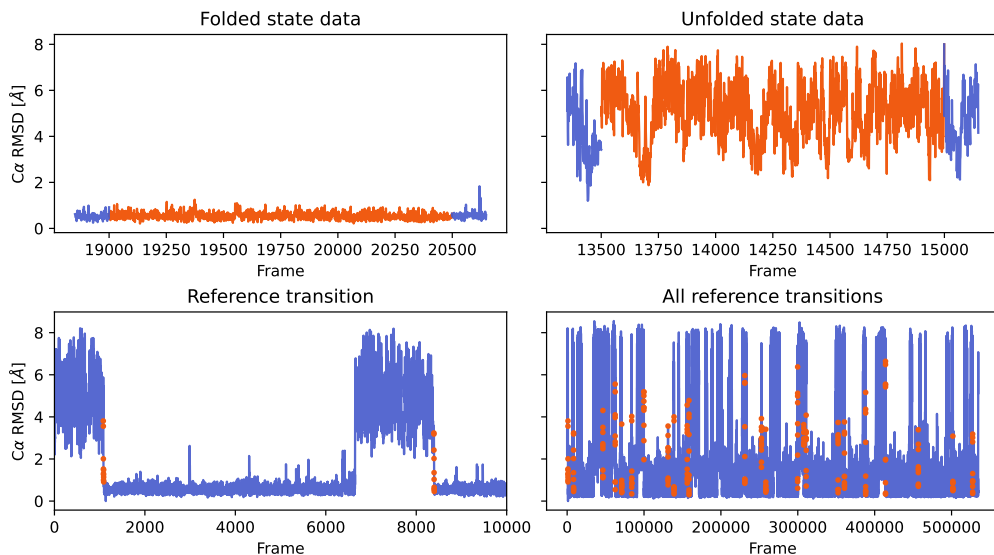


Figure S1: Frames selected from the reference trajectory are highlighted in red.

20,499th frame, while 1,500 unfolded state data points were chosen from the 13,500th to the 14,999th frame. The selected time frames are colored red in Figure S1, with 150 frames before and after the selection displayed in blue to confirm that the selection excludes transitions. The distributions of the selected points are overlaid on the TICA space in Figure 2(c) in the main text.

Extraction of reference transition configuration. We curated 240 frames from the reference trajectory encompassing folded-unfolded transitions. We define the transition as a change from C_α RMSD $> 3 \text{ \AA}$ to C_α RMSD $< 1 \text{ \AA}$ within 2 ns (10 consecutive frames) and vice versa. The selected transition frames are shown in red in Figure S1.

Geodesic interpolation. All heavy atoms of chignolin were used for interpolations. All folded and unfolded state structures were aligned to the first frame of the folded state dataset. For each interpolation calculation, two end points are selected from the metastable states and interpolated with a ratio of $t : 1 - t$, where t is an interpolation parameter sampled from the distribution $\max(\min(t \sim \mathcal{N}(0.5, 0.25), 0), 1)$.

CV model training details. The input to the models consists of the 45 pairwise contacts between the 10 C_α atoms of chignolin. To ensure that the CV has continuous derivatives with respect to atomic coordinates, each contact s_{ij} is defined using a switching function given by equation (1), where \mathbf{r}_{ij} denotes the distance between C_α atoms i and j , $d_0 = 0.0$, $r_0 = 0.8$, $n = 6$, and $m = 12$. Consequently, the contact s_{ij} can be interpreted as a continuous version of a coordination number.^{S2}

$$s_{ij} = \frac{1 - \left(\frac{\mathbf{r}_{ij} - d_0}{r_0}\right)^n}{1 - \left(\frac{\mathbf{r}_{ij} - d_0}{r_0}\right)^m} \quad (1)$$

Both the TDA and regression models were implemented as Multi-Layer Perceptrons (MLPs) with five layers in PyTorch.^{S6} The training settings for the TDA models follow those outlined by Ray et al.^{S7}, as well as the hyperparameters $\alpha = 1$ and $\beta = 250$ for the TDA loss (see eq. 4 in the main text). The target distribution parameters were set to $\{\bar{\mu}_U = -7.0, \bar{\mu}_F = 7.0\}$ and $\{\bar{\sigma}_U = 0.2, \bar{\sigma}_F = 0.2\}$ for the **TDA** model and $\{\bar{\mu}_U = -7.0, \bar{\mu}_T = 0.0, \bar{\mu}_F = 7.0\}$ and $\{\bar{\sigma}_U = 0.2, \bar{\sigma}_T = 1.5, \bar{\sigma}_F = 0.2\}$ for the **TDA_geo** and the **TDA_ref** models. We apply the following identical set of hyperparameters across all models.

N_{hidden}	Activation	Batch size	Learning rate	ℓ_2 coeff.
(45, 22, 12, 6, 3, 1)	LeakyReLU	$N_{\text{data}}/4$	1e-3	1e-5

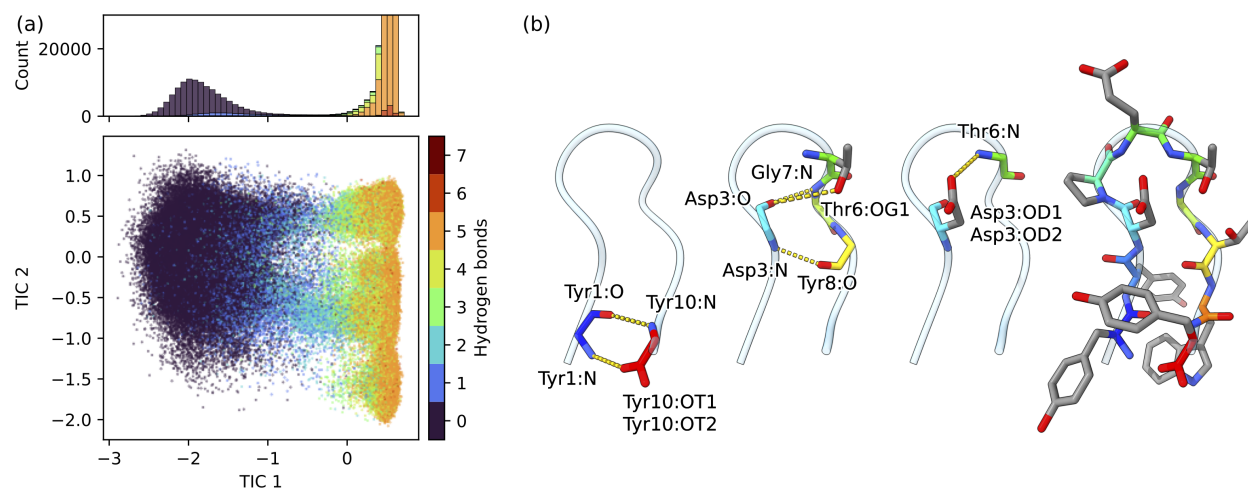


Figure S2: **(a)** Projection of conformations from the unbiased reference trajectory onto the first two time-lagged independent components (TIC 1 and 2), with the distribution along TIC 1, colored by the number of hydrogen bonds in the folded state. **(b)** Definition of the eight hydrogen bonds observed in the folded state of chignolin. The three structures to the left illustrate the donor and acceptor for each hydrogen bond, while the rightmost structure provides the complete structure of chignolin for reference. For the cases where hydrogen bonds involve two equivalent oxygens in carboxylates (Asp3:OD1/OD2 and Tyr10:OT1/OT2), a single instance is depicted in the structural diagrams.

S1.3 Structural analysis

Folded state hydrogen bonds. In addition to time-lagged independent component analysis, we devised a structure-based method to classify conformations into folded, transition, and unfolded states. We collected eight distinctive hydrogen bonds observed in the folded state, Tyr1:N–Tyr10:OT1, Tyr1:N–Tyr10:OT2, Asp3:N–Tyr8:O, Thr6:OG1–Asp3:O, Thr6:N–Asp3:OD1, Thr6:N–Asp3:OD2, Gly7:N–Asp3:O, and Tyr10:N–Tyr1:O, as depicted in Figure S2(b). The hydrogen bonds are detected in the conformation based on the two criteria: (1) acceptor and donor atom distance within 3.5 Å and (2) acceptor–hydrogen–donor angle larger than 110°. The formation of chignolin β -hairpin involves two key structural aspects: the pairing of beta sheets at the terminal regions and the turn formation.^{S8,S9} The transition from the unfolded to the folded state consist of the simultaneous formation of these two structural features, suggesting a classification threshold of two hydrogen bonds. The projection of conformations from the reference trajectory onto the slowest modes (Fig-

ure S2(a)) validates that the two metastable states can be distinguished based on the number of hydrogen bonds, with the transition region along TIC 1 aligning with the two hydrogen bonds.

S2 Additional simulation analysis

S2.1 C_α -TICA projections of the simulated trajectories

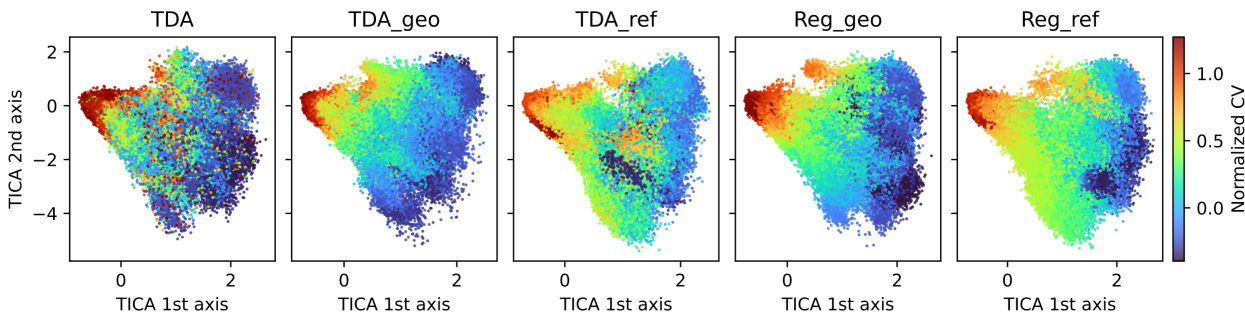


Figure S3: TICA was performed with C_α - C_α distances as inputs. Projections of the conformations from the WTM-eABF enhanced sampling trajectories using the different ML-CVs onto the first two time-lagged independent components, colored based on the normalized CV value. The CV values were scaled such that the PMF minima of the unfolded and folded basins correspond to 0 and 1, respectively.

In the main text, Figure 6 displays the TICA projections colored based on the normalized CV value, where TICA was conducted using all heavy-atom 3D coordinates as input features. Additionally, Figure S3 shows CV-colored TICA projections generated only from C_α - C_α distances. In the C_α -TICA plot, the upper-left region corresponds to the folded state, while the right region corresponds to the unfolded state. Both visualizations yield a consistent conclusion: the **TDA** models exhibit misclassification behavior, particularly by inaccurately predicting the transition state as a folded state.

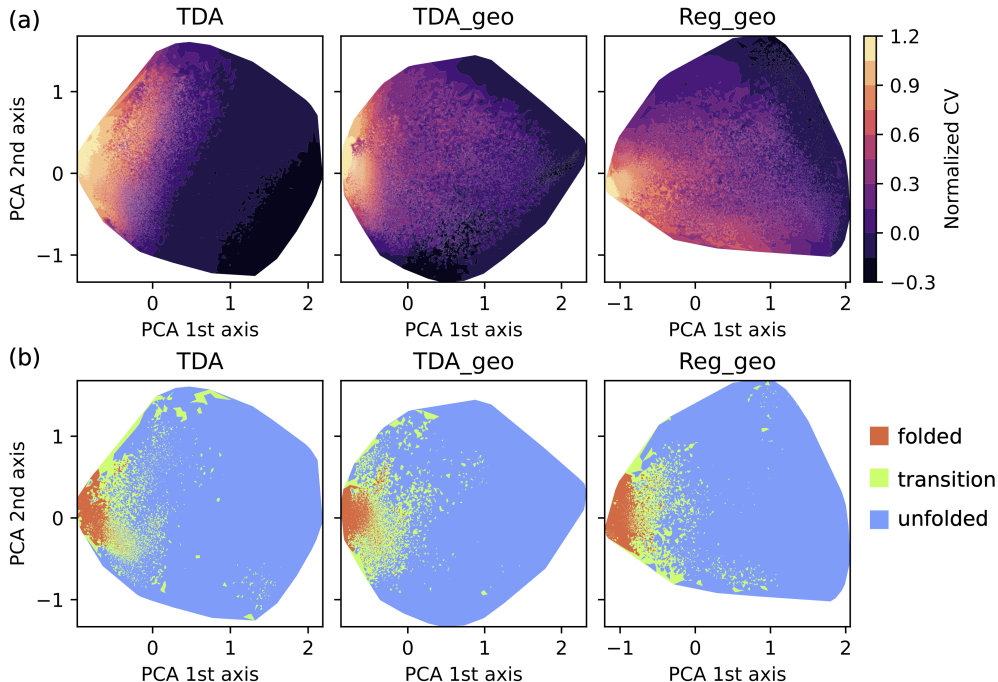


Figure S4: PCA projections of the conformations from the WTM-eABF enhanced sampling trajectories using **TDA**, **TDA_geo**, and **Reg_geo** CV models, colored by (a) the normalized CV value and (b) state labels of folded, transition, and unfolded (defined in Section S1.3).

S2.2 Analysis of the simulated trajectory in the input feature space

In this section, we further investigate how the models map input features into CV values and assess their alignment with true state labels obtained from hydrogen bond criteria. We conducted principal component analysis (PCA) using the input features to visualize simulated conformations in a reduced dimension. PCA generates eigenvectors that are linear combinations of the input features, maximizing the corresponding variance. Figure S4 displays the projection of simulated trajectories onto the first two principal components. Plots in Figure S4(a) and Figure S4(b) are color-coded based on the normalized CV value and the state labels derived from the number of hydrogen bond criteria outlined in Section S1.3, respectively.

Figure S4(b) demonstrates that in all enhanced sampling trajectories, model input features effectively differentiate between folded and unfolded states, with the TSE configurations

(two hydrogen bonds) mainly positioned between the two metastable states. Additionally, all CV models exhibit fair agreement between normalized CV values and state labels.

Ideally, the gradient of the normalized CV should align well with state transition behavior. Comparing **TDA** and the ***_geo** models reveals a much better alignment between the gradients of normalized CV and state label transitions for CVs trained with the augmented data. In the plot depicting **TDA** simulations, the gradient of CV values points diagonally, whereas state transitions mostly occur along the first principal component. This discrepancy implies suboptimal CV performance, explaining **TDA**'s inferior performance relative to ***_geo** models.

S3 Complete result analysis with the outlier included

Table S1: Mean free energy of folding (ΔF) obtained from 1- μ s WTM-eABF simulations (Figure S5) with the corresponding reference value from the long unbiased simulation, and the mean absolute error of the potential of mean force (PMF MAE) for each CV. Values in parentheses are the standard deviation from **all four independent simulations, including the outlier**. All values are reported in units of kJ/mol.

CV	ΔF	ΔF_{ref}	PMF MAE
TDA	2.65 (3.39)	-3.58	4.77 (1.00)
TDA_geo	-0.04 (2.09)	-3.53	3.29 (0.60)
TDA_ref	0.40 (4.80)	-3.58	6.27 (5.42)
Reg_geo	-5.37 (3.17)	-3.56	2.68 (0.63)
Reg_ref	-0.40 (4.98)	-3.56	3.13 (1.85)

Here, we analyze the WTM-eABF simulations without exclusion of any outlier analogous to those presented in Figure 4 and Table 1 of the main text. The results for all four independent simulations, including the outlier, are reported in Figure S5 and Table S1. While the conclusions in the main text remain valid with these results, the standard deviations of ΔF and PMF MAE are much larger, indicating that we could obtain more consistent and reliable results by removing the outlier as done in the main text.

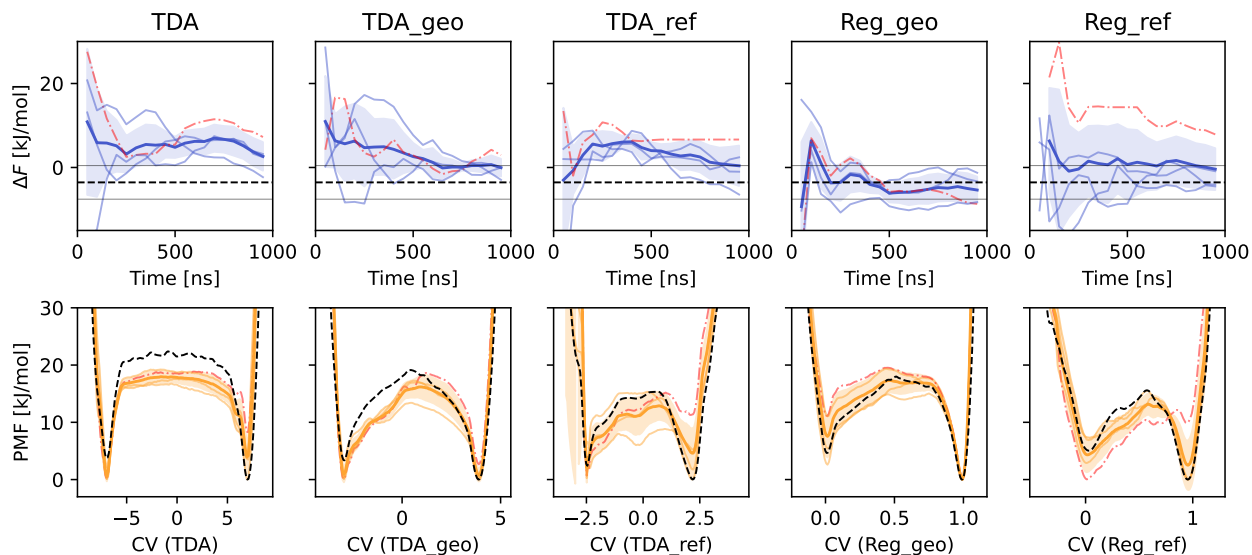


Figure S5: Convergence of the free energy difference (ΔF) between folded and unfolded state and the PMF at the end of the simulation as sampled with WTM-eABF using each CV. Top panel: Evolution of the ΔF estimate over the course of the trajectory. Solid lines indicate a ± 4 kJ/mol range (chemical accuracy) around the ΔF value obtained from the long unbiased reference run (dashed line). Bottom panel: Comparison of reference PMF obtained by projection of reference data (dotted line) and those obtained from the four $1 \mu\text{s}$ WTM-eABF simulations with the given CV. Shaded areas represent the standard deviation from **all four independent simulations, including the outlier**. Each plot is drawn with four thinner lines, each representing an individual run, with the red dash-dotted line representing the outlier.

S3.1 Outlier analysis of Reg_ref run

Here, we aim to analyze the outlier run of the simulation using the **Reg_ref** CV. The run was determined to be an outlier, since it yields a very different free energy of folding compared to the other three simulations, see the red dashed line in Figure S5), showing a significant deviation from the reference ΔF . So far, we mainly attributed the suboptimal performance of CVs to the misclassification of off-equilibrium geometries generated by enhanced sampling simulations, i.e., the ML models conflate either folded and unfolded configurations or those of the metastable states with some high-energy (off-equilibrium) geometries.

Figure S6(a) shows the evolution of the CV value over time, and each time point is colored according to the number of H-bonds formed. As established earlier (see Fig. S2, the number of H-bonds is a good auxiliary reaction coordinate for Chignolin. For most of the run, the

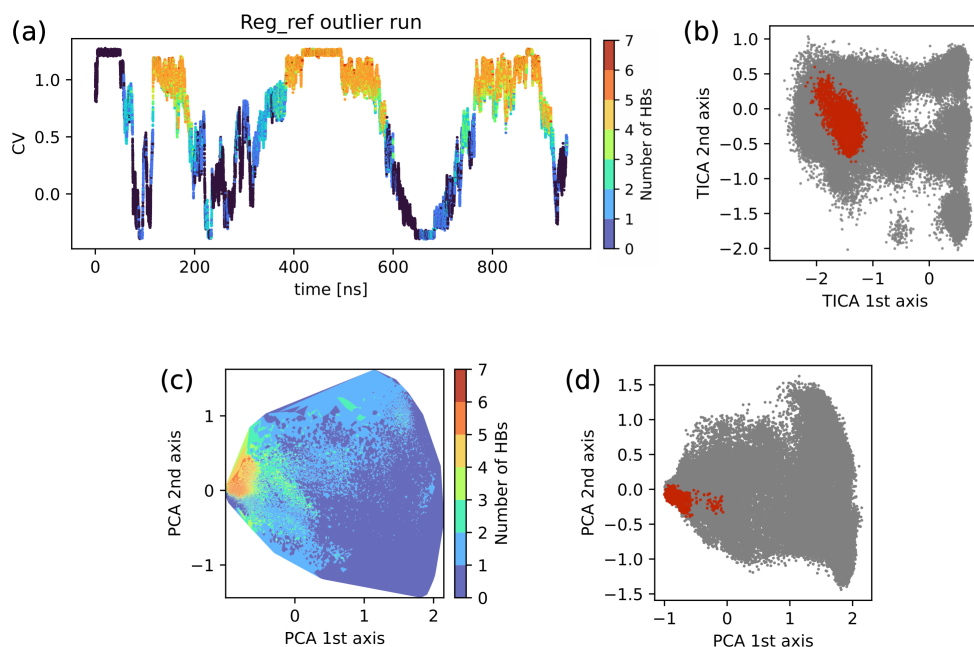


Figure S6: Analysis of the off-equilibrium geometry sampled in the outlier run of the **Reg_ref**. **(a)** **Reg_ref** CV over time of the outlier run. The initial 50 ns of the simulation were excluded as equilibration time, and 0 ns is assigned to the original 50 ns timestamp. The time frames are colored according to the number of hydrogen bonds formed. The first 50 ns are considered to be misclassified as they show poor agreement between the CV value and the number of hydrogen bonds. **(b)** TICA projections of the entire trajectory (gray) and the off-equilibrium conformations (red). **(c)** PCA projection of the input C_α -based features of the entire trajectory color-coded by number of hydrogen bonds. **(d)** PCA projection of the entire trajectory (gray) and the mislabeled conformations highlighted in red. The mislabeled conformations show significant overlap with the folded conformations on the PCA projection.

trajectory shows a good correlation between the CV value and the number of hydrogen bonds, except for the first ~ 50 ns (the part of the trajectory right after the truncated 50 ns equilibration). The all heavy-atom TICA projection in Figure S6(b) suggests that the conformations from those first 50 ns (highlighted in red) are indeed distinct from the folded state, and therefore misclassified. However, when looking at the PCA projection of the model's input features, C_α - C_α distances, we find no immediate evidence of misclassification (as shown in Figure S6(c) and (d)). The projection of conformations from the first 50 ns (in red) significantly overlaps with the projection of folded conformations. Figure S7 provides a

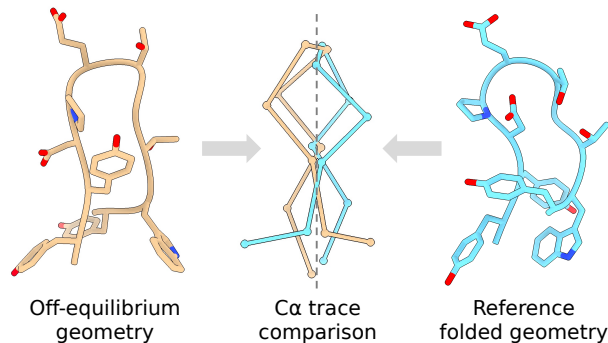


Figure S7: Comparison of an off-equilibrium geometry sampled in the outlier run of the **Reg_ref** CV to the reference folded structure of CLN025. The C_α traces of these two structures exhibit near-mirror-image relationship, implying similar C_α - C_α distance features.

structural analysis of these conformations, and further supports the conclusion drawn from PCA projection that, although the conformations are not properly folded, the C_α - C_α input features make them indistinguishable from those of the properly folded states. This likely caused the model to be unable to differentiate between these conformations based on the input feature.

The early exploration of pseudo-folded, but high-energy conformations affects the amount of bias assigned to the high-CV region (CV values close to 1), which consequently leads to higher PMF values for that region, and thus to an underestimation of the stability of folded configurations, as can be seen in Figure S5.

These results indicate that, when using the input feature set of C_α - C_α distances, the occurrence of “mirror image” conformations is infrequent yet unavoidable, i.e., it could have happened to any of the CVs, not just **Reg_ref**. Although the selection of the feature set for ML CVs is an important problem, our primary focus lies in developing a scheme to augment the conformational data for training CV models. Also, such unwanted explorations are uncommon, and most of the simulations converge to the desired result by correctly exploring folded state conformations. Hence, we conclude that, by excluding an outlier run for each CV, we were able to alleviate the effect of feature selection, as was done in our main analysis.

References

- (S1) Abraham, M. J.; Murtola, T.; Schulz, R.; Páll, S.; Smith, J. C.; Hess, B.; Lindahl, E. GROMACS: High performance molecular simulations through multi-level parallelism from laptops to supercomputers. *SoftwareX* **2015**, *1*, 19–25.
- (S2) Tribello, G. A.; Bonomi, M.; Branduardi, D.; Camilloni, C.; Bussi, G. PLUMED 2: New feathers for an old bird. *Computer physics communications* **2014**, *185*, 604–613.
- (S3) Piana, S.; Lindorff-Larsen, K.; Shaw, D. E. How robust are protein folding simulations with respect to force field parameterization? *Biophysical journal* **2011**, *100*, L47–L49.
- (S4) MacKerell Jr, A. D.; Bashford, D.; Bellott, M.; Dunbrack Jr, R. L.; Evanseck, J. D.; Field, M. J.; Fischer, S.; Gao, J.; Guo, H.; Ha, S., et al. All-atom empirical potential for molecular modeling and dynamics studies of proteins. *The journal of physical chemistry B* **1998**, *102*, 3586–3616.
- (S5) Lindorff-Larsen, K.; Piana, S.; Dror, R. O.; Shaw, D. E. How fast-folding proteins fold. *Science* **2011**, *334*, 517–520.
- (S6) Paszke, A.; Gross, S.; Massa, F.; Lerer, A.; Bradbury, J.; Chanan, G.; Killeen, T.; Lin, Z.; Gimelshein, N.; Antiga, L., et al. Pytorch: An imperative style, high-performance deep learning library. *Advances in neural information processing systems* **2019**, *32*.
- (S7) Ray, D.; Trizio, E.; Parrinello, M. Deep learning collective variables from transition path ensemble. *The Journal of Chemical Physics* **2023**, *158*.
- (S8) McKiernan, K. A.; Husic, B. E.; Pande, V. S. Modeling the mechanism of CLN025 beta-hairpin formation. *The Journal of chemical physics* **2017**, *147*.
- (S9) Sobieraj, M.; Setny, P. Granger causality analysis of chignolin folding. *Journal of Chemical Theory and Computation* **2022**, *18*, 1936–1944.